Hindawi
International Transactions on Electrical Energy Systems
Volume 2024, Article ID 6611240, 21 pages
https://doi.org/10.1155/2024/6611240

Research Article

Multiobjective Neuro-Fuzzy Controller Design and Selection of Filter Parameters of UPQC Using Predator Prey Firefly and Enhanced Harmony Search Optimization

Koganti Srilakshmi,[1] Gummadi Srinivasa Rao,[2] Katragadda Swarnasri,[3] Sai Ram Inkollu,[4] Krishnaveni Kondreddi,[5] Praveen Kumar Balachandran,[6] C. Dhanamjayulu ,[7] and Baseem Khan [8]

[1]*Department of Electrical and Electronics Engineering, Sreenidhi Institute of Science and Technology, Hyderabad, Telangana 501301, India*
[2]*Department of Electrical and Electronic Engineering, Velagapudi Ramakrishna Siddhartha Engineering College, Kanuru, Vijayawada, Andhra Pradesh, India*
[3]*Department of Electrical and Electronics Engineering, R.V.R. and J.C. College of Engineering, Guntur, AP, India*
[4]*Department of Electrical and Electronics Engineering, Dhanekula Institute of Engineering and Technology, Vijayawada, AP 521139, India*
[5]*Department of Electrical and Electronics Engineering, Chaitanya Bharathi Institute of Technology, Hyderabad, Telangana, India*
[6]*Department of Electrical and Electronics Engineering, Vardhaman College of Engineering, Hyderabad, TS 501218, India*
[7]*School of Electrical Engineering, Vellore Institute of Technology, Vellore, India*
[8]*Department of Electrical and Computer Engineering, Hawassa University, Hawassa 05, Ethiopia*

Correspondence should be addressed to C. Dhanamjayulu; dhanamjayuluc6947@gmail.com and Baseem Khan; baseem_khan04@rediffmail.com

Received 1 September 2023; Revised 22 January 2024; Accepted 22 February 2024; Published 19 March 2024

Academic Editor: Julio C. Rosas-Caro

This research introduces a unified power quality conditioner (UPQC) that integrates solar photovoltaic (PV) system and battery energy systems (SBES) to address power quality (PQ) issues. The reference signals for voltage source converters of UPQC are produced by the Levenberg–Marquardt back propagation (LMBP) trained artificial neural network control (ANNC). This method removes the necessity for conventional dq0, abc complex shifting. Moreover, the optimal choice of parameters for the adaptive neuro-fuzzy inference system (ANFIS) was achieved through the integration of the enhanced harmony search algorithm (EHSA) and the predator-prey-based firefly algorithm (PPFA) in the form of the hybrid metaheuristic algorithm (PPF-EHSA). In addition, the algorithm is employed to optimize the selection of resistance and inductance values for the filters in UPQC. The primary objective of the ANNC with predator-prey-based firefly algorithm and enhanced harmony search algorithm (PPF-EHSA) is to enhance the stability of the DC-link capacitor voltage (DLCV) with reduced settling time amid changes in load, solar irradiation (G), and temperature (T). Moreover, the algorithm seeks to achieve a reduction in total harmonic distortion (THD) and enhance power factor (PF). The method also focuses on mitigating fluctuations such as swell, harmonics, and sag and also unbalances at the grid voltage. The proposed approach is examined through four distinct cases involving various permutations of loads and sun irradiation (G). However, in order to demonstrate the performance of the suggested approach, a comparison is conducted with the ant colony and genetic algorithms, i.e., (ACA) (GA), as well as the standard methods of synchronous reference frame (SRF) and instantaneous active and reactive power theory (p-q). The results clearly demonstrate that the proposed method exhibits a reduced mean square error (MSE) of 0.02107 and a lower total harmonic distortion (THD) of 2.06% compared to alternative methods.

1. Introduction

In recent years, the integration of distributed generating sources such as wind, tidal, and solar power into the distribution network has been encouraged to reduce the load and strain on VSCs [1]. Additionally, using the unit vector generation approach for UPQC with a solar system was recommended to address difficulties related to voltage and current [2]. Subsequently, it was proposed to use multilevel UPQC with neural network-based signal generation to address PQ problems and do away with intricate p-q transformations [3]. To address the PQ problems and get rid of complicated p-q shifts, the UPQC in conjunction with the solar energy storage system with neural network-based signal production was developed [4]. In order to reduce the voltage and current THD, the fuzzy-based back propagation approach was also used for DLCV and reference signal generation [5].

The several algorithms that are now in use to regulate DLCV regulation, current control methods, harmonic separation approaches, and SHAPF functioning are described [6]. In the meantime, ANFIS was used to manage the series filter in order to handle voltage-related troubles [7]. The distributed energy system, which mixes PV and wind, was constructed to minimize load fluctuations and enable a smooth transition between the grid and the island [8]. In the meantime, the PV-connected UPQC was demonstrated to reduce the THD at voltage changes such as sag and swell by utilizing the neural network. Additionally, the suggested approach was contrasted with methods based on reactive power and SRF theories under various load scenarios [9]. To effectively manage the power and reduce the imperfections in the current signal, a combination of the grey wolf with particle swarm metaheuristic algorithms was selected to obtain the PIC's ideal gain values [10].

A feed-forward ANN was created for the wind system and solar PV systems of UPQC to maintain the DLCV steady and regulate the electricity [11]. To solve PQ issues, a novel neural network signal production method was proposed for the fuzzy controller-operated MPPT for PV-connected UPQC [12]. In order to effectively handle PQ difficulties, a UPQC custom device with a multilevel converter was connected to the fuel cell combined PV and wind systems based microgrid in the near future [13]. In the meantime, a thorough examination of various phased synchronization approaches that work well for SHAPF control and operation was conducted [14]. To minimize THD, the GWO-based PIC was recommended for different UPQC loading circumstances [15]. A novel approach was put forth to UPQC to stabilize DLCV oscillations and enable prompt, accurate fault restructuring [16]. Neuron-based controller was developed to effectively address load current THD and grid voltage issues such as swell, THD, and sag [17].

To solve the PQ problems, it was proposed to hybridize the Improvedbat and Mothflame metaheuristic optimization techniques for choosing the PIC's gain settings [18]. It was recommended that series hybrid active power filter use a fuzzy control for local distribution systems in order to successfully reduce voltage fluctuations and current THD [19]. To address PQ concerns in the distribution system, PV and SBES integrated UPQC were advised to use a soccer match optimization for the best ANNC design [20]. The PV-linked nine-level UPQC was created using an adaptive hysteresis with FLC to get voltage signals [21]. The best choice of PIC gain settings for UPQC was suggested using a soccer league in order to effectively manage both voltage fluctuations and current distortions [22]. For 5-level UPQC, the neural network pulse generation system was created to effectively handle current and voltage aberrations [23]. A novel approach was introduced to assess the level of harmonic emissions, utilizing a piecewise probabilistic high-pass filter algorithm. To begin with, a piecewise probabilistic harmonic coupled model (HCM) is employed to examine the harmonic produced by residential loads [24]. A stochastic scheduling methodology that integrates risk restrictions for an energy hub was introduced, taking into account uncertainties associated with renewable generation and load needs [25]. Furthermore, based on the established HSS model, the primary parameters are identified by analyzing the eigenvalues of the system state matrix, in conjunction with the participation factors [26]. A hybrid-modified GSA-PSO (MGSA-PSO) strategy was suggested to improve the load dispatch of a microgrid with electric vehicles by combining the gravitational search algorithm (GSA) and particle swarm optimization (PSO) algorithm [27].

A distributed optimization approach was presented that aims to reduce the overall generation cost in a dynamic economic dispatch problem (DEDP) for a hybrid microgrid network. The hybrid microgrid model was built using a combination of conventional power sources, renewable energy sources, and energy storage batteries [28]. Meanwhile, an overview of different decentralized control methods for MGs was recently published, based on research. The methods used in each study are fully described, along with their results [29]. The approach that consists of two primary components was developed: global search and local search. The global search, utilizing the modified SCO method, combines the density peak clustering (DPC) algorithm and the cooling scheduling function [30]. However, to address the issue of selecting an appropriate configuration from three available HP filter options for a specific harmonic problem, three HP filters analytically were presented in contrast to traditional optimization-based filter research [31]. Besides, a crucial concern regarding power management control in autonomous hybrid systems was suggested that there are difficulties in improving the efficiency of energy sources and backup systems, particularly when dealing with high demand or limited renewable energy production [32].

The majority of research articles employing evolutionary algorithms focused solely on fine-tuning the parameters of the traditional PIC. Furthermore, it demonstrates how the UPQC's current traditional management plans incorporate both Clarke's transformations and the complex parks. In combination with photovoltaic (PV) systems and SBES, this work provides a unique ANN control technique for UPQC that determines the optimal ANFIS controller settings using PPF-EHSA.

This work's principal contributions are as follows:

(i) Generation of reference signals for the SHAPF and SAPF of the UPQC, with LMBP-trained ANNC to prevent the usage for the complex abc to dq0 to shifting

(ii) Design of optimal ANFIS controller with PPF-EHSA for DLCV balancing in SHAPF in addition to choosing the UPQC filter parameters for THD minimization and to handle PQ troubles such as harmonics, sag, unbalances, and swell efficiently

(iii) Additionally, in order to meet the demand, minimize the stress and rating of the VSCs, and keep stable DLCV, the PV with SBES is linked to the UPQCs

(iv) Four separate test scenarios for various combinations of supply voltages, G, temperature, and load circumstances were used to validate the designed system and show how well it performed overall in terms of current THD and PF using waveform analysis

(v) Performance evaluation with GA and ACA techniques and similarly with p-q and SRF approaches

Section 1 provides an overview of the paper, followed by Section 2 outlining the UPVBSS design, Section 3 elaborating on the control scheme, Section 4 discussing the acquired results, and Section 5 concluding the paper.

2. Development of Suggested UPQC System

Figure 1 displays the suggested UPVBSS schematic diagram. Here, the battery is linked to a DC capacitor via a buck-boost converter (B-B-C) and PV via a boost converter (B-C). Besides, V_{abc} denotes the grid voltage, and V_{S_abc} resembles the grid phase voltage. The load voltage and current are denoted by the symbols V_l and i_l. L_S stands for grid-side inductance, whereas R_S stands for grid-side resistance. UPQC is the acronym for the combination of series and shunt VSCs. In order to address grid-side voltage-related problems, SAPF uses the injecting transformer to supply the proper compensating voltage V_{se}. The RL filter consists of two parts: the inductor L_{se} and the resistor R_{se}. The SHAPF is connected to the grid by resistance R_{sh}, which interfaces with inductance L_{sh}. The goal of SHAPF is to minimize the harmonics and to keep DLCV constant with a brief settling time by injecting a sufficient compensatory current through the point of common coupling (PCC).

2.1. Modelling of Solar and Battery Systems. By adding solar and batteries to the UPQC's DC-link, the utility's demand for converters is reduced, negating the need for high ratings. In this case, B-C is utilized to increase the solar system's and buck-boost converters' output. The battery connected to the DC-link is charged and discharged using B-B-C to control the DLCV when loads vary. The controller for the PV and batteries is described because the modeling of these systems is already accessible in the literature [5]. Equation (1) provides the power demand () for the proposed approach.

$$P_{PV} \pm P_{BSS} = P_L. \tag{1}$$

2.1.1. PV System. The solar radiation is converted into electrical power by the SPG structure. The quantity of series and parallel connections made to these PV cells is a determining factor in the necessary solar generation. The PV model used in this study is from the Simulink library. To extract the highest yield from modules, however, the MPPT algorithm (incremental conductance) was selected. The PV system's (PPV) power is determined by the following equation:

$$\mathrm{P_{PV}} = \mathrm{V_{PV}} \times \mathrm{i_{PV}}. \tag{2}$$

In this section, the terms "i_{PV}" and "V_{PV}" stand for the current and voltage that a solar panel produces, respectively. In this study, the *P* and *O* are offered as MPPT to manage the B-C duty cycle (D) and generate the maximum output power.

2.1.2. SBES. The DLCV is stabilized by the SBES in support with B-B-C. Equation (3) expresses the state-of-charge-of-the-battery (SOCB).

$$\mathrm{SOCB} = 80\left(1 + \int i_{BSS}\,\mathrm{dtQ}\right). \tag{3}$$

The output generated by PV will determine whether a battery is in the charging or discharging state by meeting the top and bottom bonds given by the following equation:

$$\mathrm{SOCB_{min}} \le \mathrm{SOCB} \le \mathrm{SOCB_{max}}. \tag{4}$$

The i^{ref}_{dc} is computed by minimizing the DLCV error $V_{dc,err}$ by a PIC. The battery error reference current i_{BS,err^*} is calculated using PIC. Where $i_{BS,err}$ reflects the mismatch between the reference current of battery i^{ref}_{BS} obtained from the filter and the i^{ref}_{dc} retrieved from it. The controller of the developed system with the hybrid algorithm is given in Figure 2, and the graphical layout of the power flow is shown in Figure 3. The power flow between grid, load, solar, and battery is clearly illustrated in the forms of waveforms in results and discussions as case studies.

2.2. DC Capacitance (C_{dc}). Equation (5) can be used for determining the C_{dc} value [5].

$$C_{dc} = \frac{\pi * i_{sh}}{\sqrt{3}\omega V_{cr,pp}}. \tag{5}$$

The V^{ref}_{dc} is selected within the range of ratings allowed by the recommended approach. The selection of C_{dc} is influenced by shunt corrective current and voltage ripple ($V_{r,pp}$).

2.3. Inductor for Shunt Converter. By shunt inductor (L_{sh}), the shunt converter is connected to the system. Equation (6) gives the frequency of switching, ripple current, and DLCV.

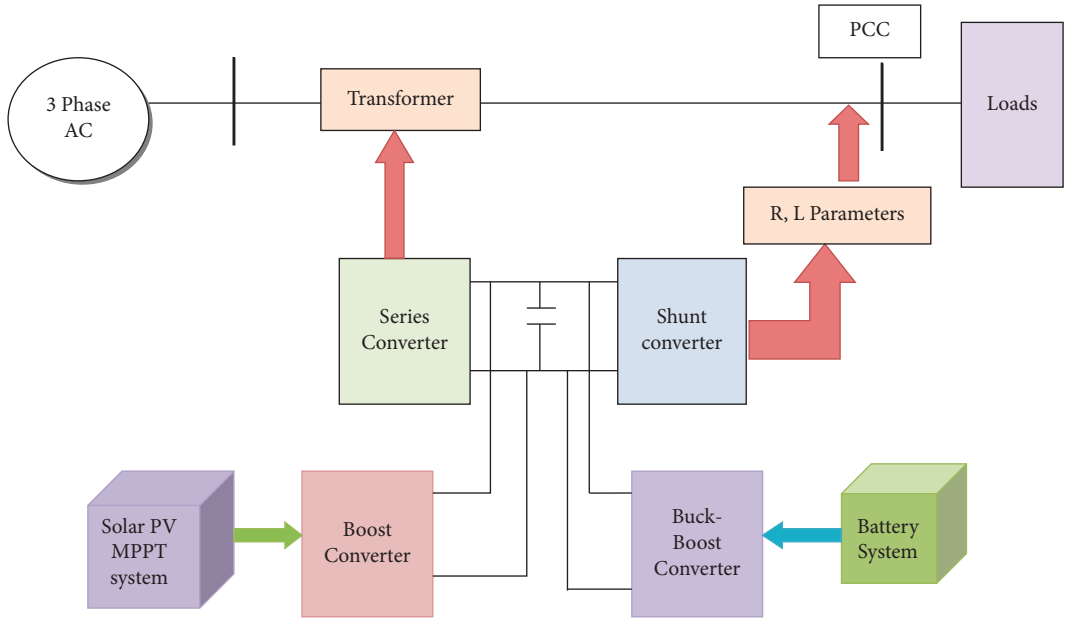

Figure 1: Schematic representation of UPQC.

$$L_{sh} = \frac{\sqrt{3}\, m\, V_{dc}}{12\, a_f\, f_{sh}\, I_{cr,pp}}. \tag{6}$$

Peak-to-peak ripple current ($I_{r,pp}$) determines the magnitude of L_{sh} considering that the frequency of switching (f_{sh}) is 10 kHz, the modulation depth (m) is 1, and the overloading factor (a_f) is 1.5.

2.4. Inductor for Series Converter with Isolation Transformer. The series VSC is connected to the grid using a power injection transformer, and the design requirements are given in the following equations:

$$K_{se} = \frac{V_{L-L}}{\sqrt{3}\, V_{se}}, \tag{7}$$

$$L_{se,min} = \frac{\sqrt{3}\, m\, V_{dc}\, K_{se}}{12\, a_f\, f_{se}\, I_{cr,pp}}, \tag{8}$$

with a 10 kHz frequency of switching, and the series inductance is dependent on the ripple current.

3. Artificial Neural Network Control

VLDC typically fluctuates in tandem with changes in the distribution side dynamic load. However, before the system can resume regular operation, it needs to swiftly revert to its initial condition (VLDC). Here, firing pulses are generated using the suggested ANNC to manage the PWM hysteresis-current of the shunt VSC.

3.1. Shunt VSC. By introducing corrective current, SHAPF aims to eliminate current waveform distortions and stabilize DLCV in fault and transient loading conditions.

3.1.1. Optimal Selection of ANFIS Parameters for DLCV Stability. It is advised that the ANFIS keeps the DLCV constant. The proposed ANFIS combines the capabilities of an ANNC and FLC to create a smart combination controller. However, to keep the DLCV steady, the acquired DLCV and the selected reference DLCV are compared, and the variation in error (CE) and its output error (E) are taken into account as inputs. As seen in Figure 4, the inputs given into the neural network are first trained based on the triangular membership to yield optimal results. The ANFIS is primarily composed of five layers: fuzzification is the first layer, and its outputs are fuzzy MSF, which are determined by the following equation:

$$\begin{aligned} &\mu_{Ai}(x), i = 1, 2, \\ &\mu_{Bj}(y), j = 1, 2. \end{aligned} \tag{9}$$

Here, $\mu_{Ai}\mu_{Bj}$ resembles the memberships received as the output from the 1st layer.

The triangular membership is expressed by the following equation:

$$\mu_{Ai}(x) = \max\left(\min\left(\frac{x - a_i}{b_i - a_i}, \frac{c_i - x}{c_i - b_i}\right), 0\right), \tag{10}$$

where b_i is the fuzzy set i's point of greatest support and x_{min}, x_{max} (lower and upper bonds) is the range (world of discourse) of x. Under normalization, −1 and 1 are regarded as lower and upper bonds in this work. The subsequent items are classified as inputs and outputs: positive small (POSS), positive big (POSB), positive medium (POSM), negative small (NEGS), negative big (NEGB), negative medium (NEGM), and zero (ZERO). The MF's inputs and outputs are shown in Figure 5.

Where the AND operator is used in the second layer (weighting of fuzzy rules) to determine the strength of firing

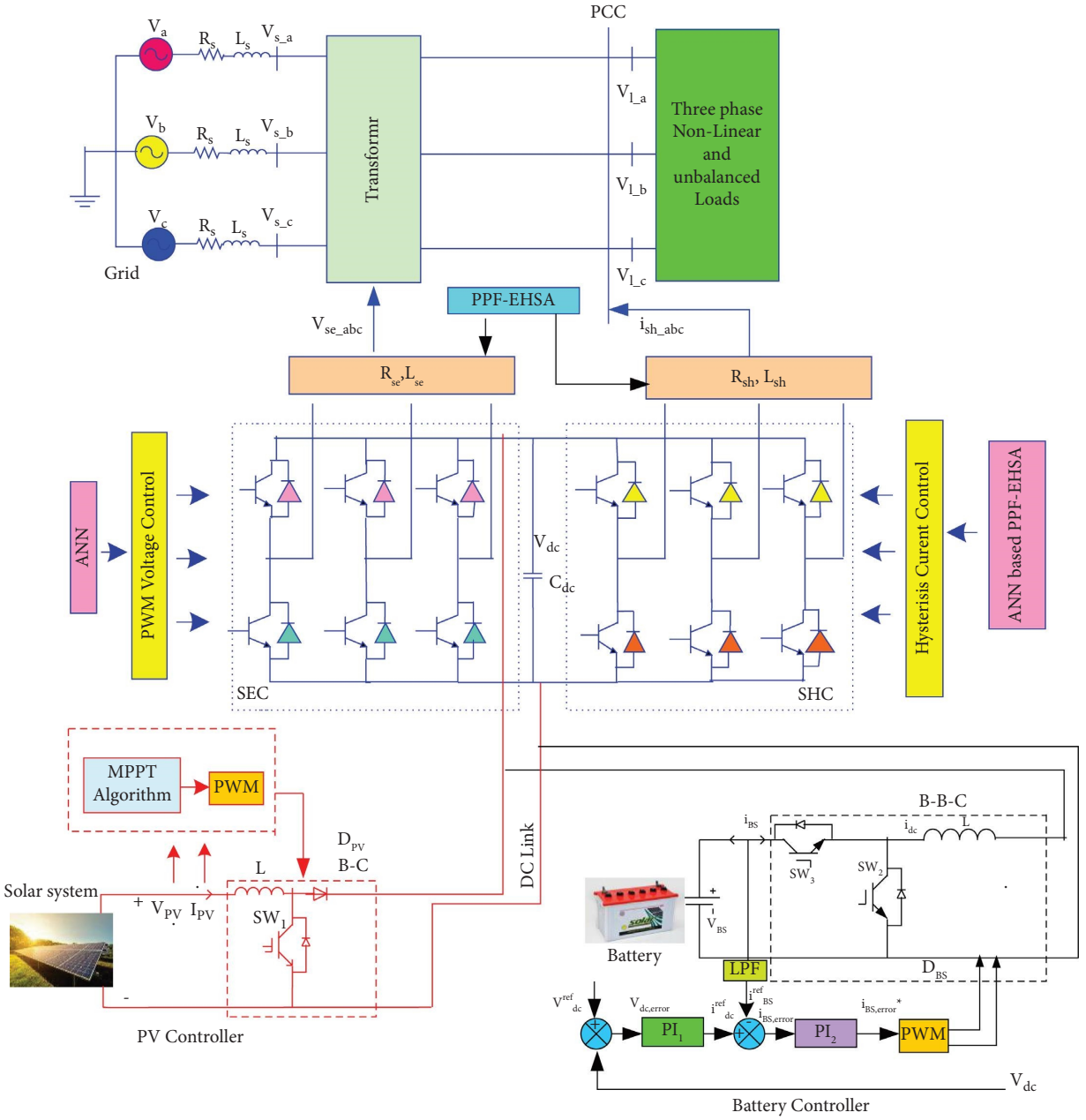

Figure 2: Controller system with hybrid algorithm.

by using the MSF in the first layer, the output of which is determined by the following equation:

$$w_k = \mu_{Ai}(x) * \mu_{Bj}(y) i, j = 1, 2. \tag{11}$$

In the third layer, which receives data from the preceding layer, values are normalized. By calculating the ratio of the firing strength (true values) for the k^{th} rule to the total firing strength of all rules, every node achieves normalization, as shown by the following equation:

$$\overline{w_k} = \frac{w_k}{w_1 + w_2} k = 1, 2. \tag{12}$$

By using the inference variables (p_k, q_k, r_k) in the fourth layer (defuzzification), the ANNC can adapt to itself. The output of this process is provided by the following equation:

$$\overline{w_i} f_i = \overline{w_i}(p_k u + q_k v + r_k). \tag{13}$$

Finally, in equation (14), at the fifth layer, all the inputs are added to generate the necessary total ANFIS output.

$$f = \sum_i \overline{w_i} f_i. \tag{14}$$

Figure 6 displays the layout of ANFIS. The goal of the hybrid algorithm that combines PPFA and EHSA is to optimize the a_i, b_i, and c_i of membership in order to

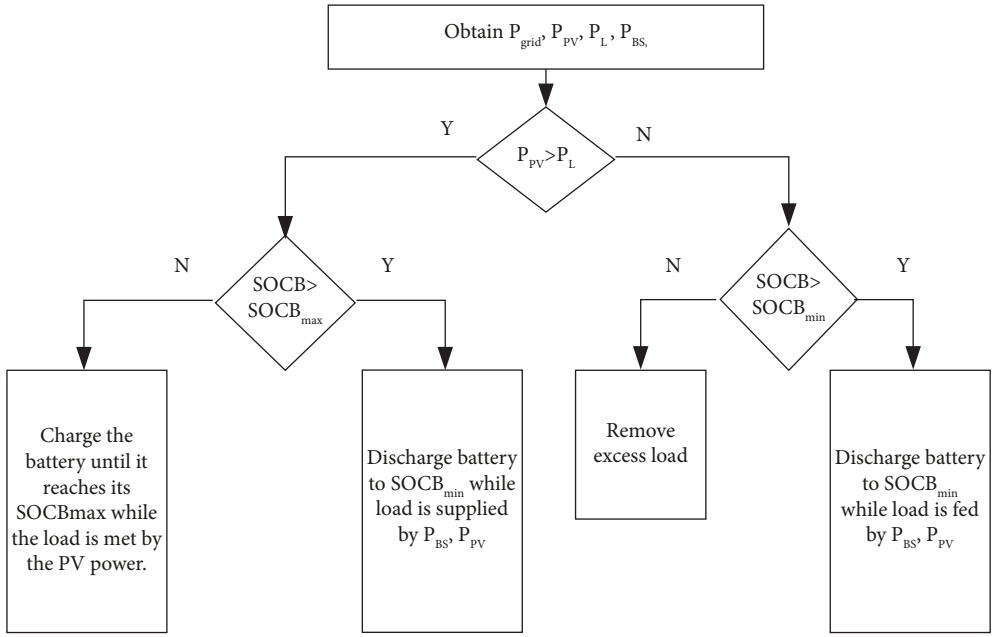

Figure 3: Power flow.

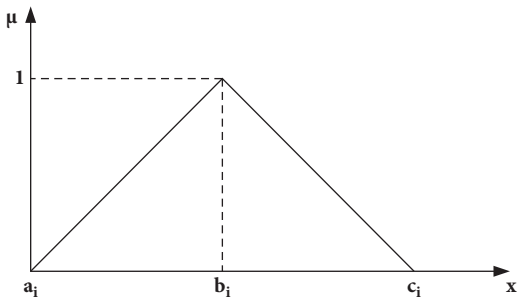

Figure 4: Triangular membership.

minimize learning errors and enhance the overall performance of the ANFIS controller. The goal of the problem is to evaluate the fitness function provided by equation (15) in order to achieve the objective (obj), which is expressed as MSE.

$$\begin{aligned} \text{Maximize} F &= \frac{1}{1+\left(\text{obj}_1, \text{obj}_2\right)}, \\ \text{obj}_1 &= \text{MSE} = \frac{1}{n}\sum_{p=1}^{m}\left(O_p - \overline{O}_p\right)^2, \\ \text{obj}_2 &= \text{THD} = \frac{\left(\sqrt{I_2^2 + I_3^2 + ...I_n^2}\right)}{I_1}. \end{aligned} \tag{15}$$

Here, $\overline{o}$ is the desired result, o is the output that was obtained, and m is the number of instances. The fundamental and harmonic components of current are resembled by I_n, I_1. A detailed discussion of the suggested hybrid algorithm is given.

3.1.2. PPFA. The firefly algorithm is motivated by the illuminated habits of the collection of fireflies. First, an arbitrary set of fireflies is generated in the space. Each firefly here represents the required solution, which is entirely dependent upon the parameters chosen for control. Each firefly (y) represents the control parameters whose limits are expressed as follows:

$$y^k(\min) \le y^k \le y^k(\max); k = 1, 2... nd, \tag{16}$$

where nd = total variables

The fireflies' bioluminescent communication is used by this program to control their movement. Every firefly is drawn to the illumination of the opposing firefly and tries to move in that direction. The firefly's illumination function (F) provides the ideal solution for the selected issue. This approach computes the illuminating function iteratively and modifies their placements accordingly. Equation (17) represents the attraction between the i^{th} and j^{th} fireflies.

$$\beta_{ij} = \beta_0 \exp\left(-\gamma r_{\text{ij}}^2\right), \tag{17}$$

where r_{ij} is the Cartesian distance, as calculated by equation (18) between the firefly i^{th} and j^{th}.

$$r_{\text{ij}} = \left\| y_i - y_j \right\| = \sqrt{\sum_{k=1}^{\text{nd}}\left(y_i^k - y_j^k\right)^2}. \tag{18}$$

The i^{th} firefly moves toward the other j^{th} firefly in the group and changes its position if BF_j is bigger than BF_i according to the following equation:

$$y_i(t) = y_i(t-1) + \beta_{\text{ij}}\left(y_j(t-1) - y_i(t-1)\right) + \alpha(\text{rand} - 0.5). \tag{19}$$

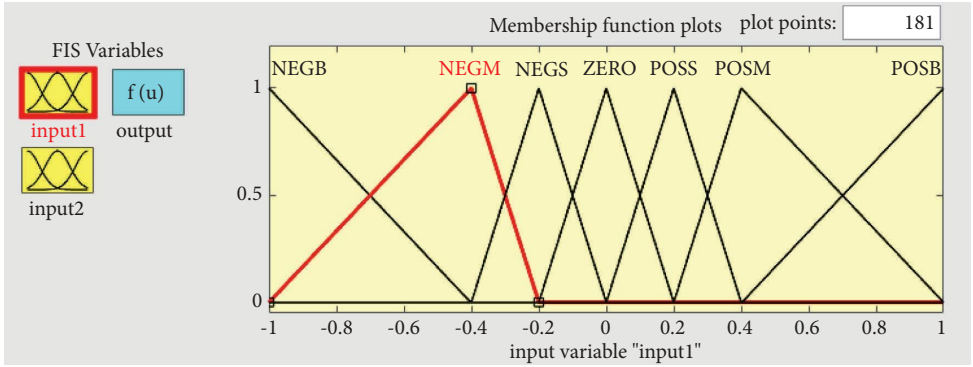

(a)

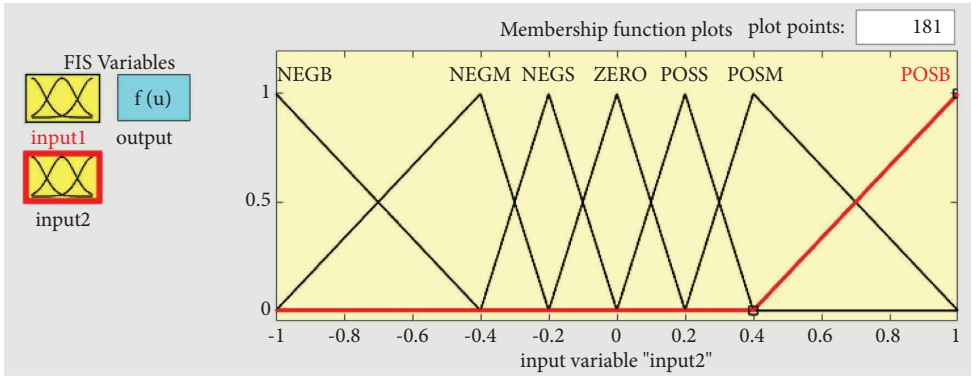

(b)

Figure 5: Fuzzy MSF for E and CE. (a) Membership for E. (b) Membership for CE.

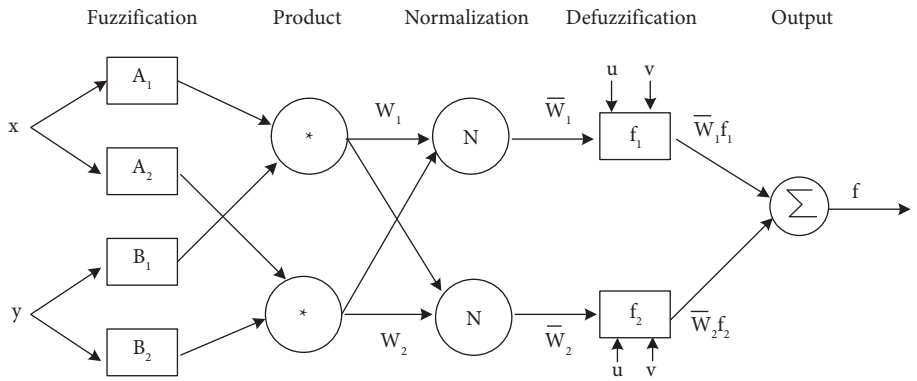

Figure 6: Layout of ANFIS.

Fireflies (prey) encounter challenges in remaining at their desired locations when pursued by predators. Instead, they seek new locations that are devoid of predators and potentially more favorable. The predatory behavior aids fireflies in efficiently exploring the search area. The predation by predators is regulated by a modest hunting probability factor η, and the predators are characterized based on the least optimal solutions.

$$y_{\text{pred}}(t) = y_{\text{worst}}(t) + \rho\left(1 - \frac{t}{T^{\max}}\right). \tag{20}$$

The fireflies consistently distance themselves from predators, a behavior that can be represented through modeling.

$$\begin{aligned} y(t+1) &= f(t) + \rho.e^{-|d|}, \text{ if } d0\rangle, \\ y(t+1) &= f(t) - \rho.e^{-|d|}, \text{ if } d\langle 0. \end{aligned} \tag{21}$$

The improved firefly algorithm prevents the swarm from converging to a suboptimal point in the search space. Instead, it enhances exploration capabilities and compels the population to settle at the globally optimal solution.

3.1.3. EHSA. This metaheuristiciterative strategy, which takes inspiration from artists' improvisational approach to music, explores problem space to find the best global solution thatmaximizes the chosen fitness function (F) while meeting the problem constraint. The problem space is defined by a harmony memory (HM), which consists of several candidate solutions, each representing a harmony, as outlined in the following equation:

$$\mathrm{HM};= \begin{bmatrix} h_1^1 & h_2^1 & \cdots & h_N^1 \\ h_1^2 & h_2^2 & \cdots & h_N^2 \\ h_1^3 & h_2^3 & \cdots & h_N^3 \\ \vdots & \vdots & & \vdots \\ h_1^{\mathrm{HMS}} & h_2^{\mathrm{HMS}} & \cdots & h_N^{\mathrm{HMS}} \end{bmatrix}, \quad h_i \longrightarrow [h_{i1}, h_{i2}, \cdots, \cdots, \cdots, \cdots, h_{im}]. \tag{22}$$

The goal of the optimization is to minimize error by optimally selecting the MSF parameters a_i, b_i, and c_i in the ANFIS. The harmony fitness function (F), which is derived from the goal as the selected problem as shown in equation (15), evaluates the quality of each harmony. As stated in equation (23), an improvised harmony $h^{'} = (h_1', h_2', \cdots, h_N^{'})$ is produced by comparing a random number with the HM adjusting rate (HMAR) value.

$$\begin{aligned} &\text{if (rand ( ) < HMAR)} \\ &\quad h_i' \leftarrow h_i' = \left(h_i^1, h_i^2, \cdots, h_i^{\mathrm{HMS}}\right) \\ &\text{else} \\ &\quad h_i' \leftarrow h_i' \in \{h_i(\min) \leftrightarrow h_i(\max)\} \\ &\text{end.} \end{aligned} \tag{23}$$

Here, 0~1 is a random number and rand (). Equation (24) modifies the pitch of every variable in the improved harmony according to the pitch tuning rate (PTR).

$$\begin{aligned} &\text{if (rand ( ) < PTR)} \\ &\quad h_i' \leftarrow h_i' \pm \text{rand ( )} \times \mathrm{BW} \\ &\text{else} \\ &\quad h_i' \leftarrow h_i' \\ &\text{end.} \end{aligned} \tag{24}$$

Here, BW stands for bandwidth. The poorest harmony in the HM is substituted by the new harmony $h^{'}$ if the improved harmony vector $h^{'}$ is better than the worst harmony.

The conventional harmony search optimization may fall into suboptimal traps during problem-solving due to the absence of a jumping mechanism. To address this issue, this section introduces a mechanism utilizing poorly composed music that induces dissonance. Referred to as the dissonance-avoiding mechanism, it draws inspiration from the predator-prey optimization concept, enabling the newly generated harmony to jump away from unfavorable harmonies. If the spontaneous combination of musical tones resembles the unpleasant combination of tones in the harmonic minor scale, the newly created combination of tones may result in discord. The new harmony must be altered to ensure its dissimilarity from bad harmony by augmenting the Euclidean distance (γ) between them using the following equation:

$$\begin{aligned} h_i' &\leftarrow h_i' + \alpha.\, e^{-\gamma}, \nearrow if\ \gamma > 0, \\ h_i' &\leftarrow h_i' - \alpha.\, e^{+\gamma}, \nearrow if\ \gamma < 0. \end{aligned} \tag{25}$$

Here, α resembles the dissonance factor. The process of generating new harmony is iterated until convergence. Every fly modifies its location, HMAR, and PTR in HSA based on the F value, which helps the convergence to accurately signify the global optimal solution. The process is executed until it reaches the maximum number of iterations ($T^{\max}$). The HS method offers notable benefits such as fast convergence, minimized parameter changes, and straightforward implementation. Nevertheless, it exhibits other shortcomings, such as suboptimal convergence speed and premature convergence. Table 1 presents the parameters chosen for the suggested optimizations and their subsequent comparison.

Begin

Step 1. Collect the data

Set the parameters: define γ, $t = 1$; $T^{\max}$, β_0, α at $r = 0$; HMAR, BW, PTR, HMS, number of fireflies.

Step 2. Assess the Brightness function F.

Step 3. While $t < T^{\max}$

Arrange the fireflies based on their brightness;

for $i = 1$: Give value for i^{th} firefly (all fireflies) do

Execute simulation and obtain THD using equation (17)

for $j = 1$: Give value for j^{th} firefly (all fireflies) do

Execute simulation and obtain THD using equation (17)

if ($F_j < F_i$) then

By calculating equation (19), move firefly j toward i using equation (22);

else

for $k = 1$: (all harmonies) do

if (rand ( ) < HMAR) then

Utilize equation (23)

if (rand ( ) < PTR) then

Utilize equation (24)

Apply equation (25) to avoid bad harmony

end if

end for k

end if

if r and $<\eta$

Hunt jth-firefly by equation (20) and (21)

Modify attractiveness; Modify brightness; end for j

end for i

Table 1: Algorithm parameters.

Technique	Variable	Value
PPFA	nf	30
	T^{max}	150
	β_0	0.97
	α	0.5
	γ	0.92
EHSA	HMS	42
	Pitch tuning rate	0.09
	HMAR	0.93
	T^{max}	150
	BW	0.13
GA	Population	50
	Alpha	0.85
	T^{max}	150
	Mutation	0.1
ACA	T^{max}	150
	Initial pheromone (τ)	$1e-06$
	Global pheromone decay rate	0.9
	Pheromone constant	1
	Decay rate	0.5

Get the brightness F.

Rank the fireflies, and the one with the highest brightness is the sought-after optimal solution;

$t = t + 1$;

Step 4. end

while End.

3.2. Neural Network for Reference Signal Production. Figure 7 illustrates the proposed artificial neural network (ANN) controller for the shunt filter. The ANNC configuration includes the input layer (IPL), hidden layer (HIL), and output layer (OPL). The objective of IPL is to collect the given data and transmit it to the HIL. The weights on the interconnected linkages between the IPL and HIL are subsequently multiplied by this quantity. At this location, mathematical calculations are carried out with a pre-established inclination towards HIL. Ultimately, the OPL is employed to resolve the discoveries. To ensure accurate results, the link weights are modified during training through an evaluation of the error. Thus, the LMBP training strategy is employed to achieve expedited convergence.

Figure 7 designates the reference currents ($i^{ref}_{sh\_a}$, $i^{ref}_{sh\_b}$, $i^{ref}_{sh\_c}$) as the desired data, while the load currents (i_{l_a}, i_{l_b}, i_{l_c}) and DC loss component (Δi_{dc}) are treated as the input. Figure 8 illustrates the expected BP structure for the 200 neurons in the HIL system, which is utilized to generate the reference current signal. The shunt VSC is believed to generate the required gating signals through the operation of a hysteresis controller within the ±0.25 A and ±0.5 A range.

3.3. Series Converter. The principal function of a SAPF is to reduce grid voltage disruptions and ensure a constant load voltage by generating compensating voltages. Figure 9 illustrates the suggested control system for the VSC series. The supply voltage signal (V_{s_a}, V_{s_b}, and V_{s_c}) is considered as input data for generating the reference voltage signals ($V^{ref}_{se\_a}$, $V^{ref}_{se\_b}$, and $V^{ref}_{se\_c}$), which are considered as target data for the neural network. Figure 10 provides the configuration of a neural network with 200 neurons in the HIL. PWM is employed to generate the sequence of VSC gating pulses.

4. Results and Discussion

The proposed UPVBSS with ANNC was implemented using MATLAB 2016a. The appendix provides the system's and UPQC's configurations. Four test cases were selected to show the functionality of the proposed ANNC-controlled PPF-EHSA. These test cases involved different rectifier-based nonlinear loads, balanced and unbalanced, as well as varying source voltages. Additionally, the test cases included circumstances such as swell, disturbance, and sag, which were influenced by changing irradiation (G).

The test cases are presented in Table 2. In case 4, V_S is selected as an unbalanced phase supply, while, for cases 1–3, it is chosen as a balanced phase supply. The investigation focused on cases 1 and 2, specifically examining concerns related to balanced sag and swell. Besides, the unbalanced condition is assessed in case 3. This study focuses on minimizing THD by optimizing the selection of filter parameters R_{se}, R_{sh}, L_{se}, and L_{sh}. The limits for these parameters are chosen as (0–10), (0–0.5), (0.01–10), and (0.01–10), respectively. The major objective is to improve PF and ensure a constant DLCV by optimizing the selection of parameters for the ANFIS. The performance of the proposed ANN-based PPF-EHSA is demonstrated by comparing the results with GA and ACA approaches. Figure 11 presents the convergence plot of MSE for the suggested technique, genetic and ant colony algorithms in relation to case 1. The PF is determined by applying equation (26) to the obtained THD.

$$\mathrm{PF} = \cos\theta * \frac{1}{\sqrt{1 + \mathrm{THD}^2}}. \tag{26}$$

For the first case study, the balanced voltage source is used to analyze the behavior of the SAPF. According to Figure 12(a), 30% of balanced sag and swell occurred in the range of 0.2 to 0.3 seconds, and another occurrence happened between 0.4 and 0.5 seconds in the VS system. ANNC accurately detects and responds to changes in voltage, efficiently providing the necessary compensating voltage to provide a constant load terminal voltage. To assess the performance of the suggested approach's SHAPF, we examined load 1 and load 4. The load current shape in Figure 12(b) is nonsinusoidal and balanced due to the presence of harmonics. The proposed solution rectifies the deficiencies in the existing waveform, resulting in a reduction of the THD of the current waveform from 17.74% to 2.06% and an increase in the PF to 0.9898. In addition, as illustrated in Figure 12(c), the proposed approach regulates the constant DLCV under a fixed 1000 W/m^2 light and a constant temperature of 25°C. Figure 12(d) demonstrates that the suggested system adequately meets the load demand

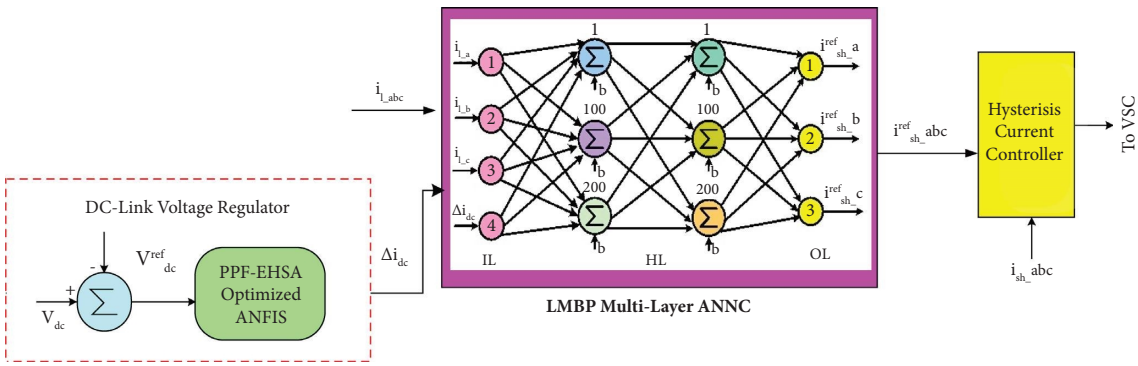

Figure 7: Shunt VSC controller.

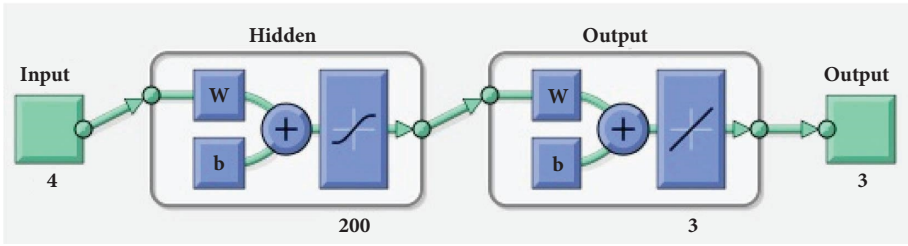

Figure 8: NNC for reference signal generation of current.

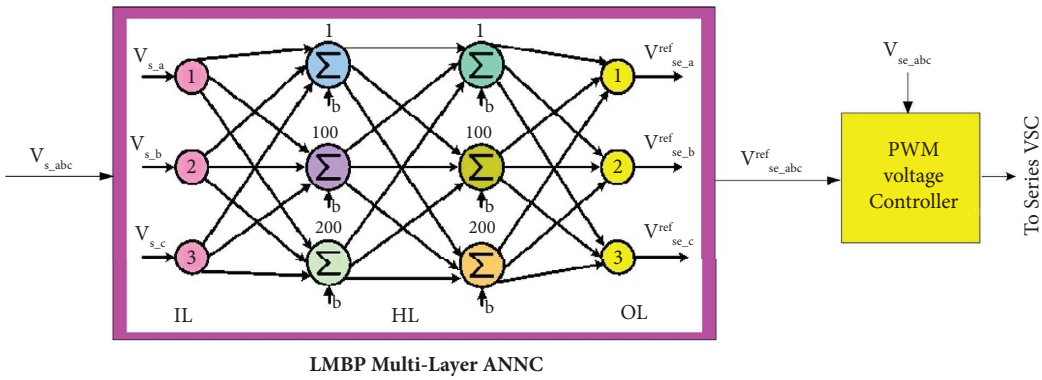

Figure 9: Series VSC controller.

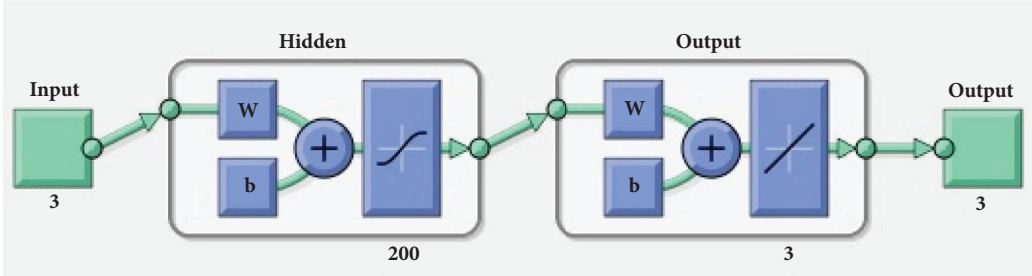

Figure 10: Structure of ANNC for reference voltage generation.

In case study 2, which is similar to Case 1, the V_S is chosen to be balanced. To verify the functionality of the series filter, a disturbance is introduced from 0.6 to 0.7 seconds. Nevertheless, as depicted in Figure 13(a), ANNC accurately identifies the disruption in the grid voltage and resolves it by introducing the required compensatory voltage. As a result of the simultaneous operation of loads 1, 2, and 3, the i_l waveform was determined to be

Table 2: Test cases chosen.

Circumstance	Case 1	Case 2	Case 3	Case 4
Balanced V_S	✓	✓	✓	
Steady voltage				✓
Unbalanced V_S				✓
Current	✓	✓	✓	✓
Balanced V_{Sag} and V_{Swell}	✓			
Balanced disturbance		✓		
Unbalanced, V_{Sag}, V_{Swell}, and disturbance			✓	
Irradiation of 1000 w/m^2	✓		✓	
Variable irradiance		✓		✓
Variation in load				✓
Load 1: balanced 3 phase bridged rectifier load: $L = 1$ mH and $R = 10\,\Omega$	✓	✓	✓	✓
Load 2: balanced 3 phase bridged rectifier load: $L = 2$ mH and $R = 20\,\Omega$		✓		✓
Load 3: unbalanced 3 Φ RL branch load: $R_1 = 10\,\Omega$, $R_2 = 20$, $R_3 = 15\,\Omega$, $L_1 = 1.5$ mH, $L_2 = 3.5$ mH, and $L_3 = 2.5$ mH		✓	✓	✓
Load 4: balanced active reactive power load: $P = 500$ W and $Q = 9000$ Kvar	✓		✓	

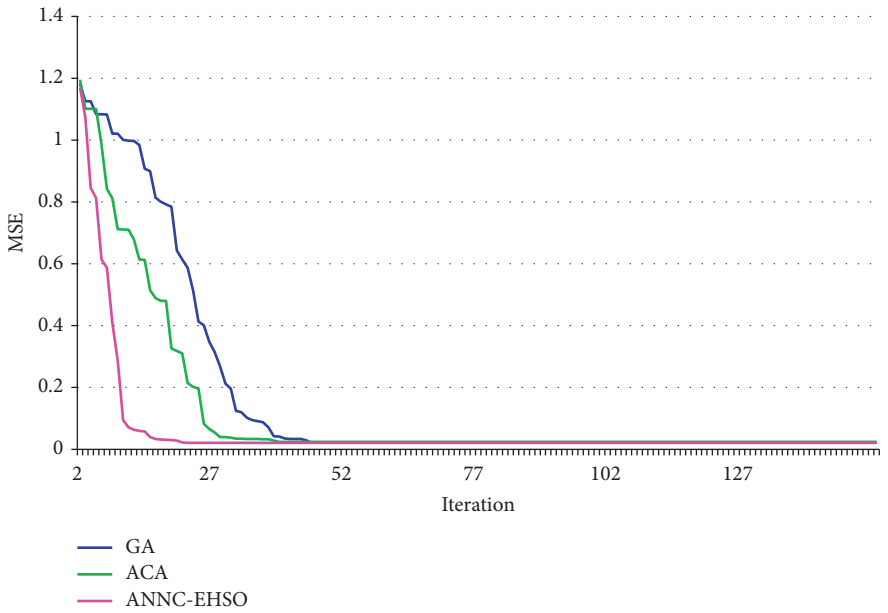

Figure 11: Comparison of convergence characteristics for case 1.

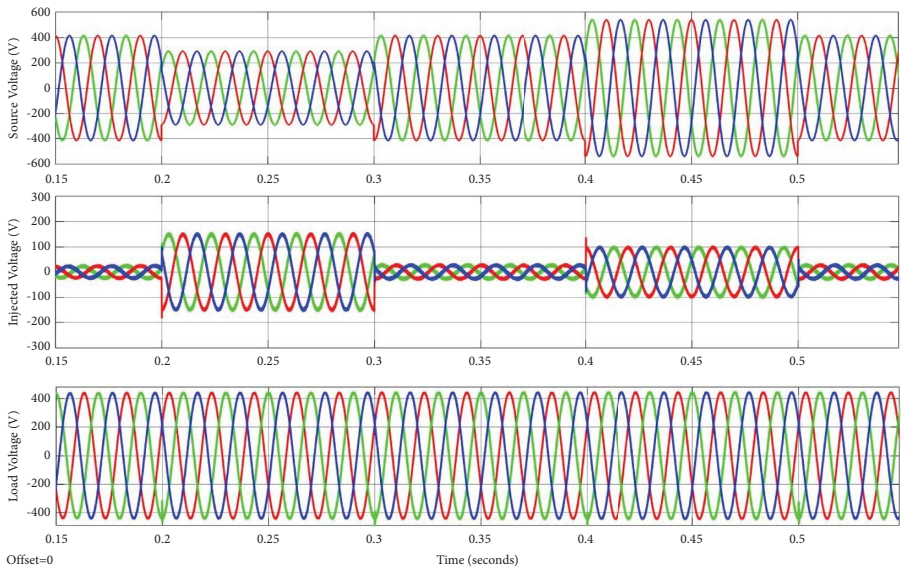

(a)

Figure 12: Continued.

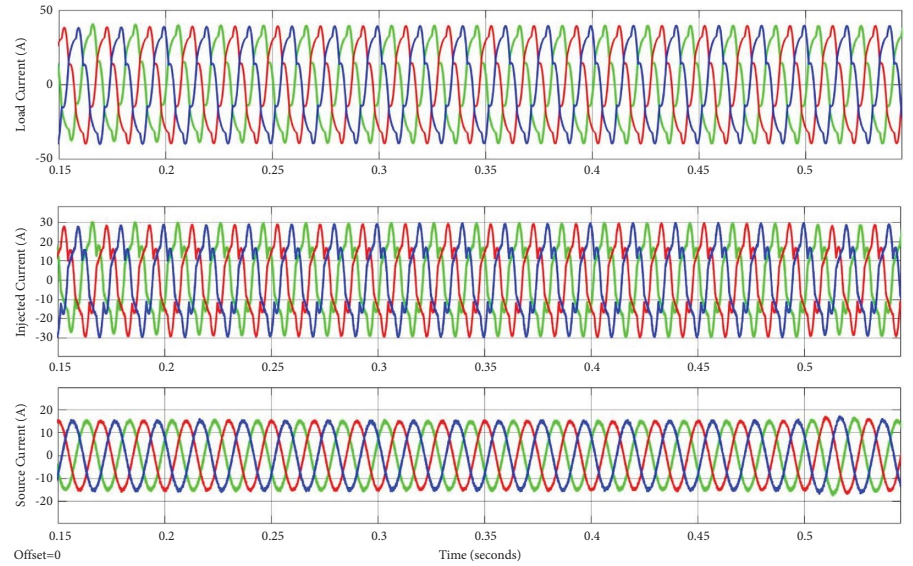

(b)

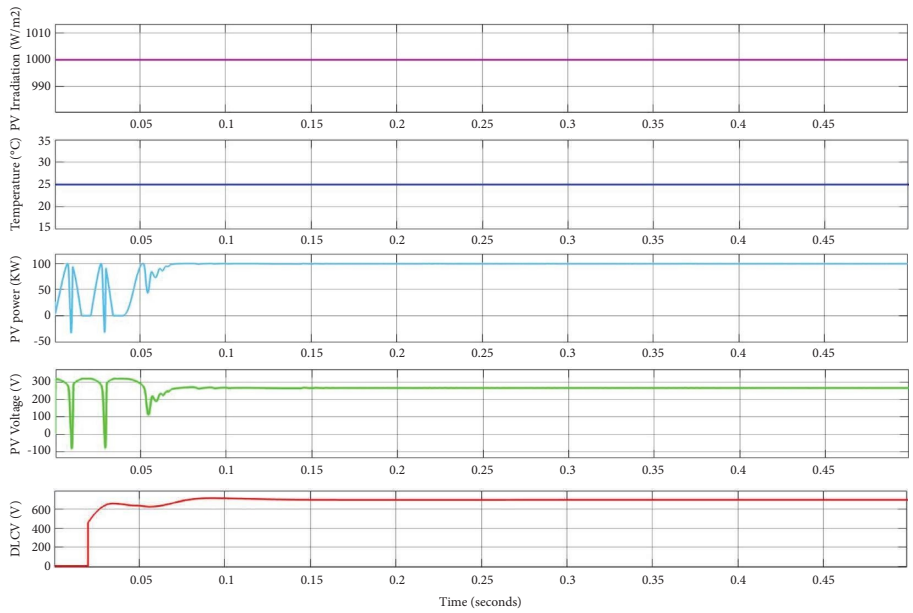

(c)

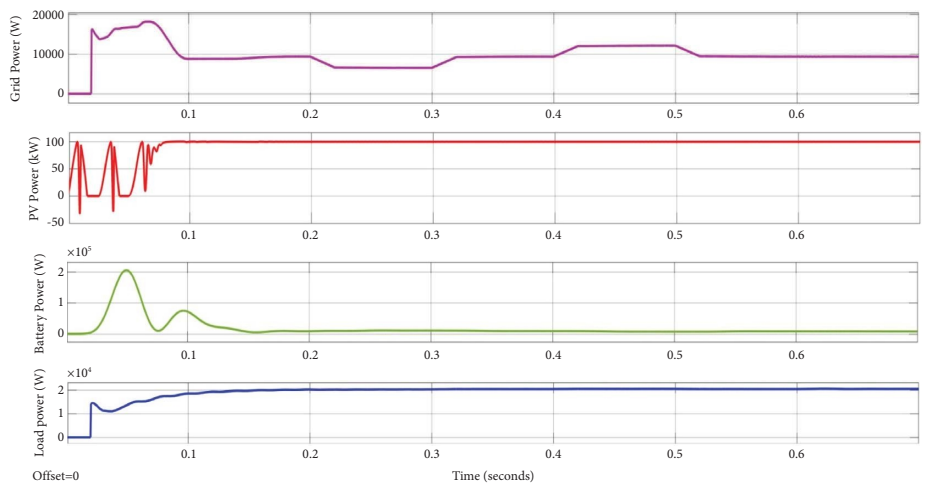

(d)

FIGURE 12: Waveforms for case study one. (a) V_S, V_{se}, and V_l. (b) i_l, i_{sh}, and i_s. (c) G, temperature, P_{PV}, V_{PV}, and V_{dc}. (d) Grid power, PV power, battery power, and load power.

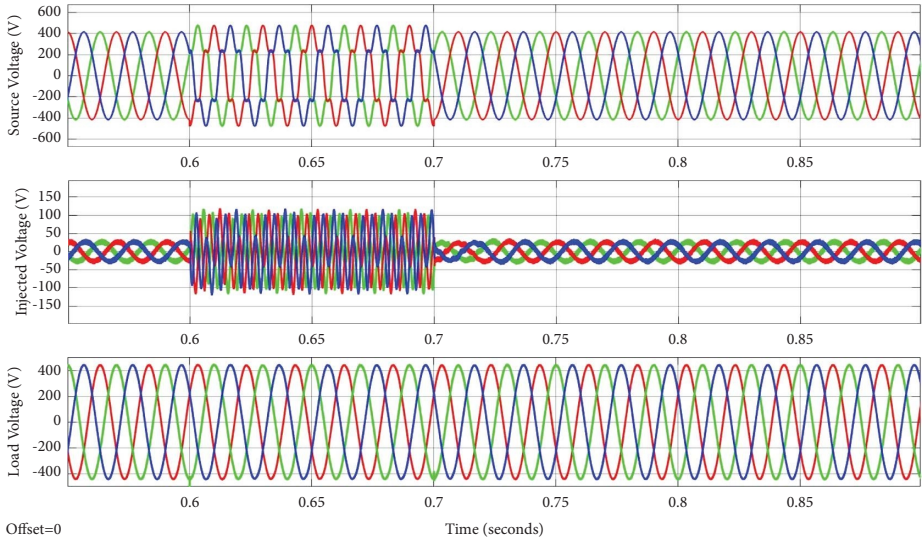

(a)

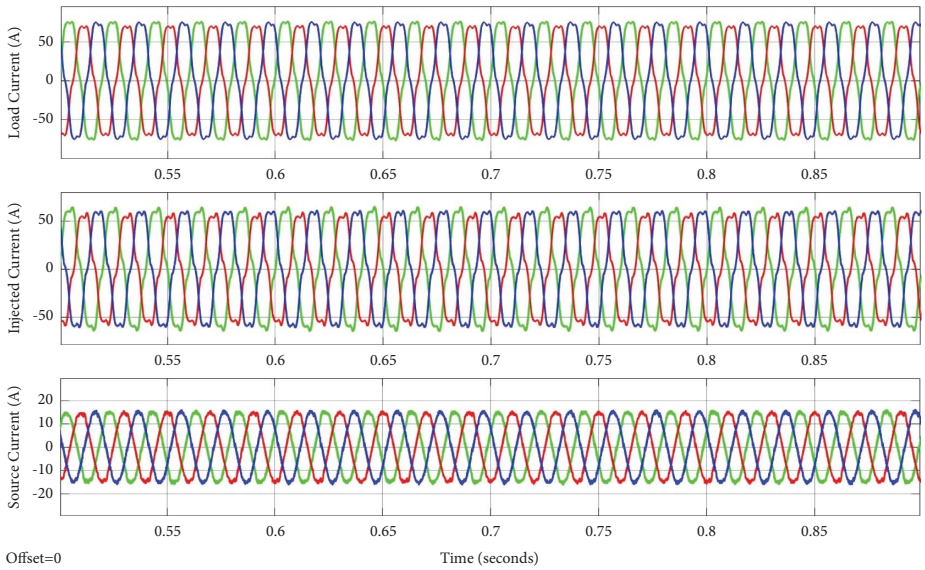

(b)

Figure 13: Continued.

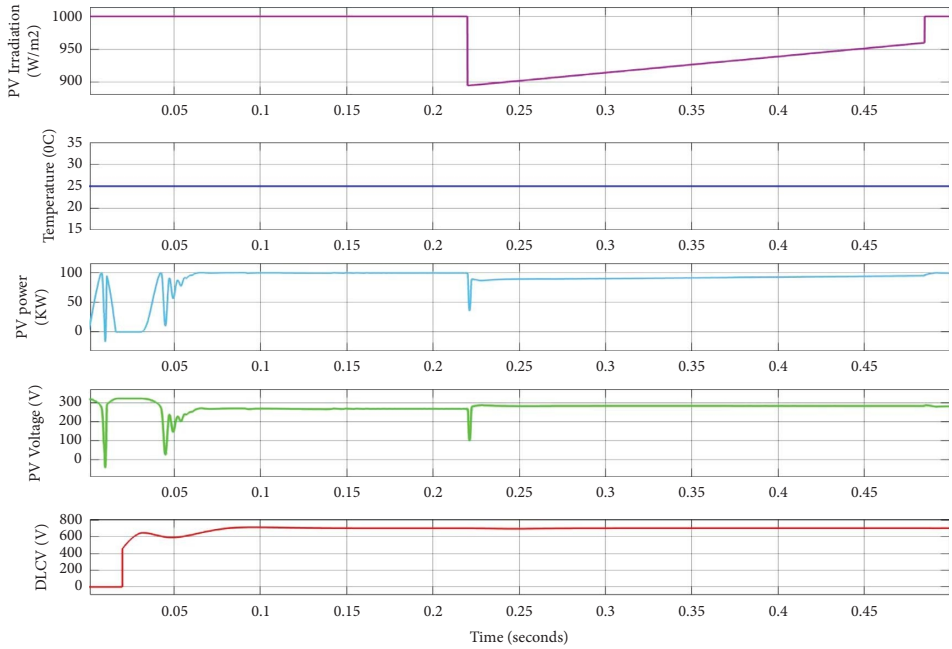

(c)

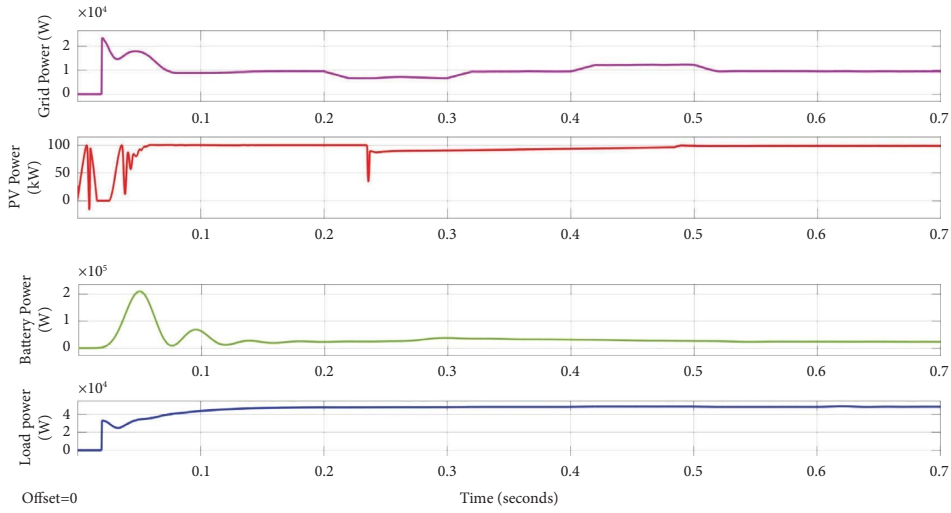

(d)

Figure 13: Waveforms for case study two. (a) V_S, V_{se}, and V_l. (b) i_l, i_{sh}, and i_s. (c) G, temperature, P_{PV}, V_{PV}, and V_{dc}. (d) Grid power, PV power, battery power, and load power.

nonsinusoidal and imbalanced, as depicted in Figure 13(b). The proposed technique effectively reduces the current THD from 21.54% to 4.72%, a significantly lower value compared to alternative solutions. Additionally, the PF improves to almost unity. In this scenario, both variable irradiation and load variation are taken into account while maintaining a constant temperature of 25°C. The proposed technique maintains a constant DLCV as G fluctuates, as depicted in Figure 13(c). Additionally, it effectively provides power to the load, as demonstrated in Figure 13(d).

In the third case study, the V_S is deliberately adjusted to achieve a balanced state. This balanced state is then subjected to a 30% increase in sag and swell, as well as an external disturbance, in order to verify its performance. Nevertheless, as depicted in Figure 14(a), ANNC accurately identifies the asymmetrical phase voltage fluctuation, voltage increase, and disruption and resolves it by introducing the required compensatory voltage. Furthermore, in order to assess the efficiency of the SHAPF, loads 1 and 4 were consolidated, and at the 0.7-second mark, load 3 was added. Consequently, the resultant waveform exhibited significant contamination, imbalance, and amplified magnitude, as depicted in Figure 14(b). The proposed method rectifies the disparities in the current signal. The PF rises to 1, and the THD of the current signal decreases from 3.76% to 27.44%. Furthermore, Figure 14(c) demonstrates that the proposed controller effectively keeps the DLCV constant while

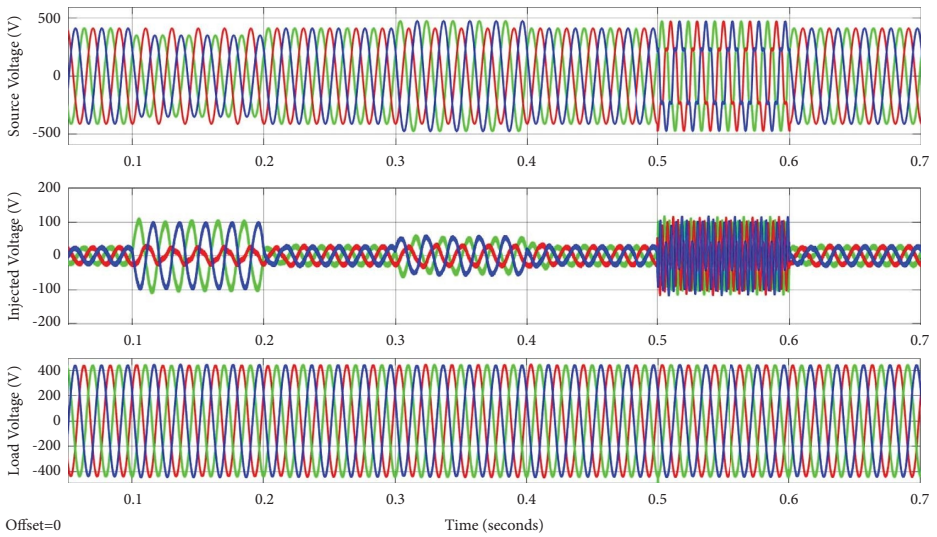

(a)

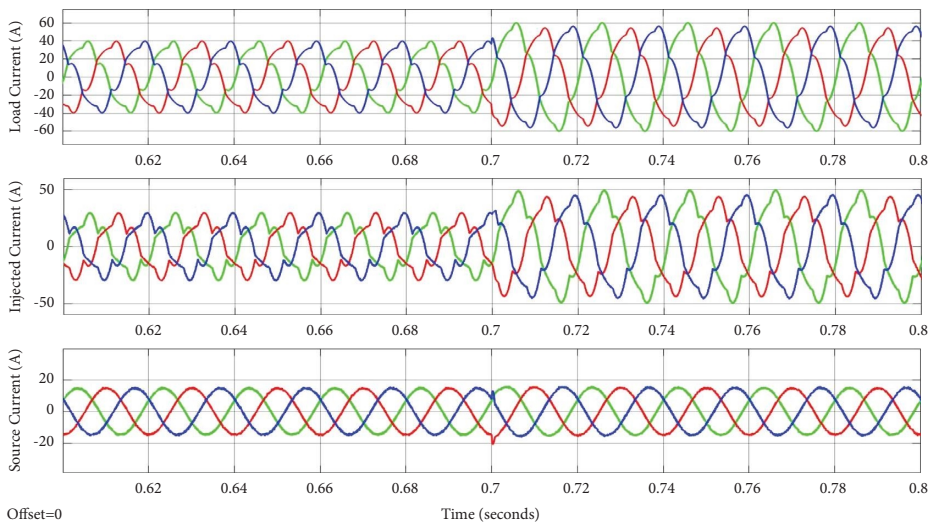

(b)

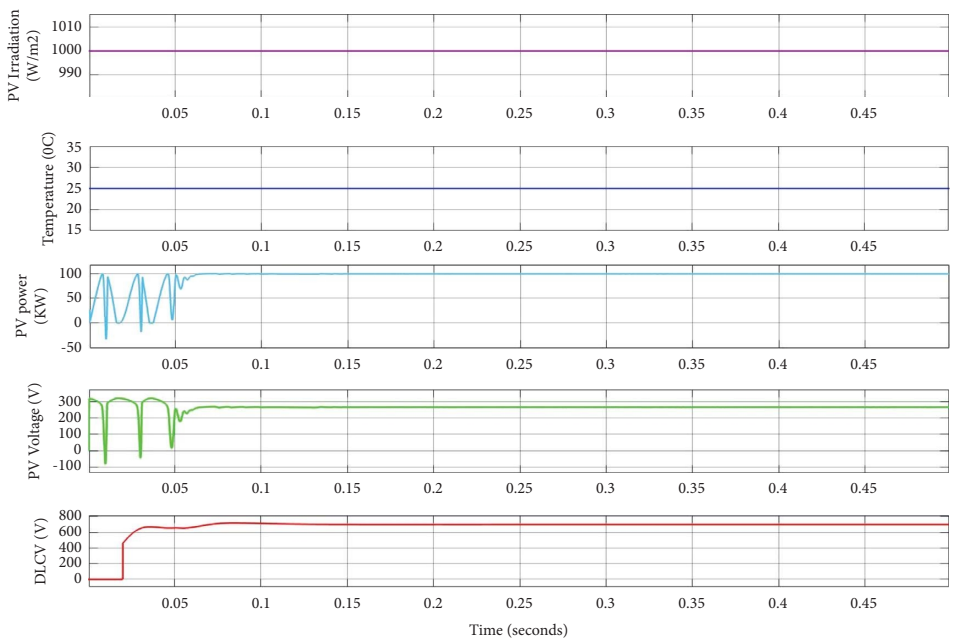

(c)

Figure 14: Continued.

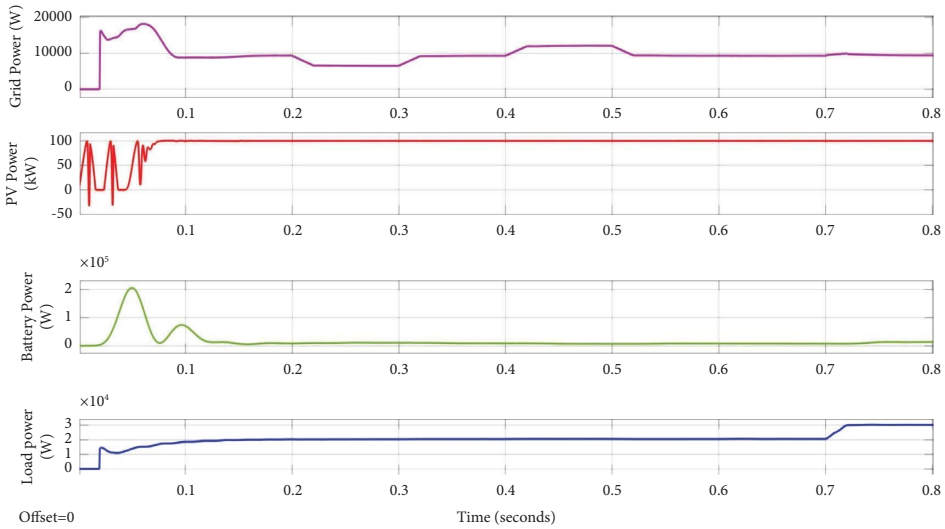

(d)

Figure 14: Waveforms for case study three. (a) V_S, V_{se}, and V_l. (b) i_l, i_{sh}, and i_s. (c) G, temperature, P_{PV}, V_{PV}, and V_{dc}. (d) Grid power, PV power, battery power, and load power.

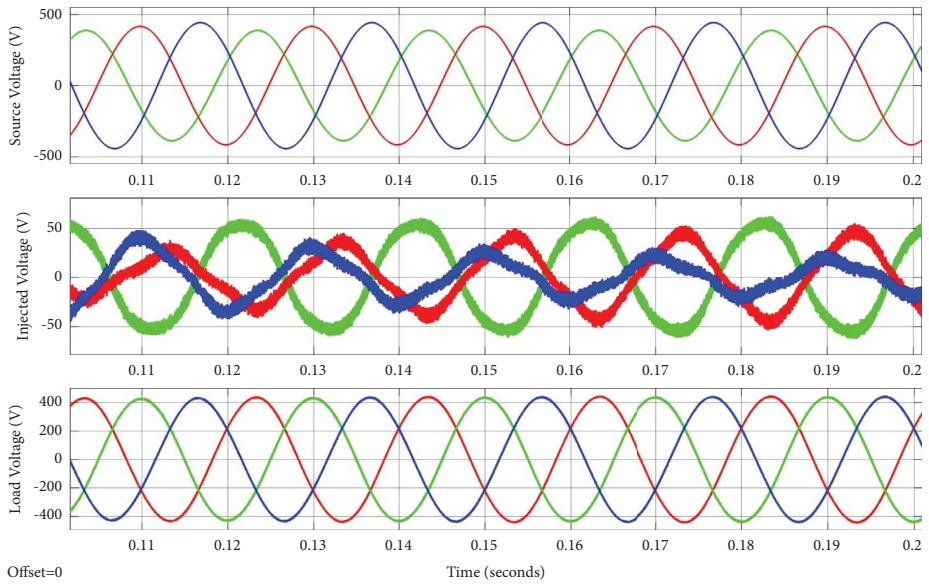

(a)

Figure 15: Continued.

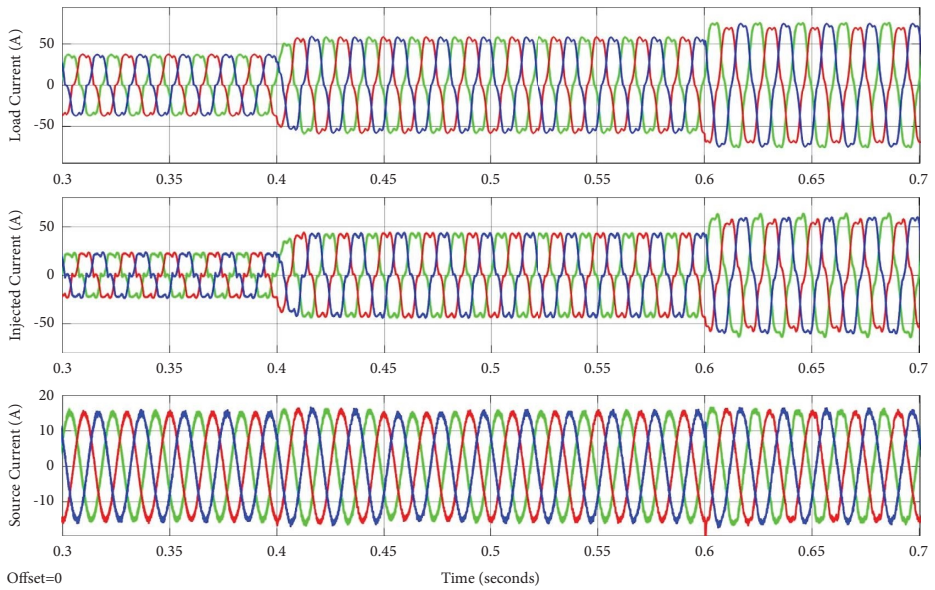

(b)

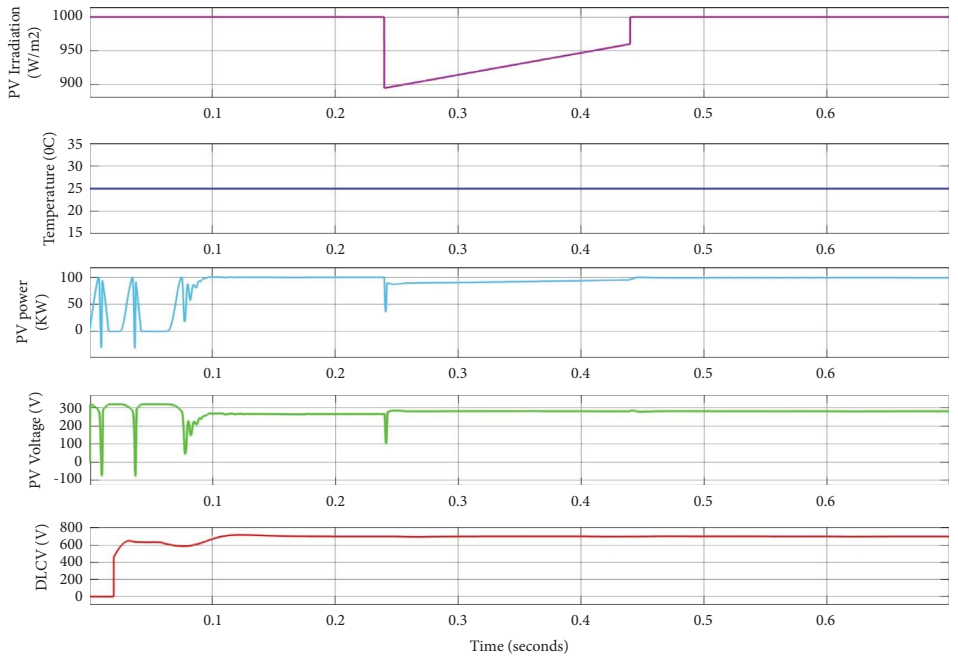

(c)

Figure 15: Continued.

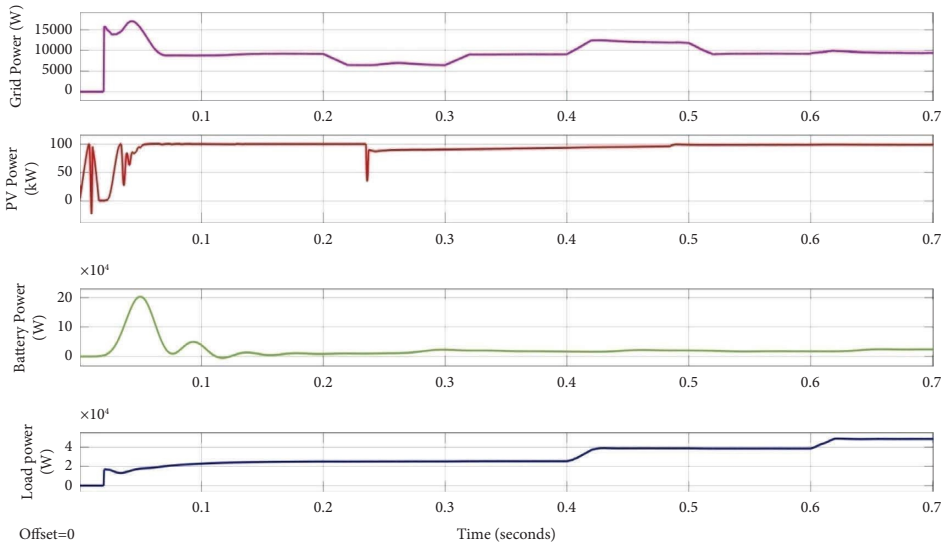

(d)

FIGURE 15: Waveforms for case study four. (a) V_S, V_{se}, and V_l. (b) i_l, i_{sh}, and i_s. (c) G, temperature, P_{PV}, V_{PV}, and V_{dc}. (d) Grid power, PV power, battery power, and load power.

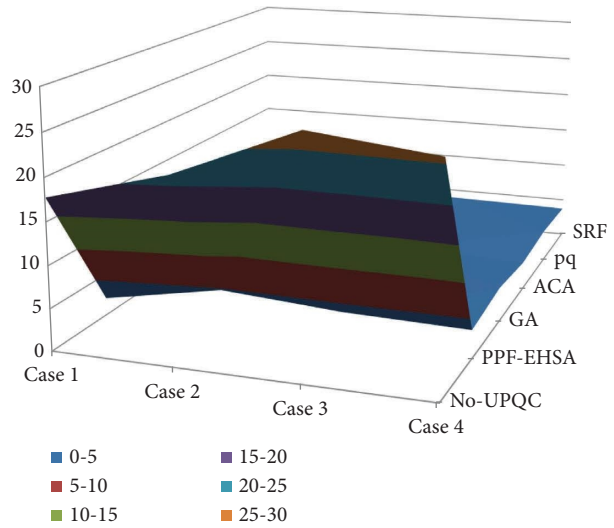

FIGURE 16: THD comparison for case studies.

simultaneously meeting the load requirements specified in Figure 14(d).

In the fourth case study, it is believed that the V_S is unequal in phases. However, the system identifies the imbalances and effectively rectifies them, as depicted in Figure 15(a). In this case, loads 1 to 3 were sequentially connected by incrementally applying to the existing load at time intervals of 0.1 seconds to 0.4 seconds, 0.4 seconds to 0.6 seconds, and 0.6 seconds to 0.7 seconds, respectively. Consequently, the i_l waveform was determined to be contaminated and lacking equilibrium, as depicted in Figure 15(b). The THD decreased from 25.86% to 3.43%, and the PF rose to a value of 1. Furthermore, as illustrated in Figures 15(c) and 15(d), the proposed controller effectively ensures a consistent DLCV despite changes in load, variations in irradiation, and a constant temperature of 25°C. It successfully fulfills the required demand.

Figures 16 and 17 present a comparison of the THD and PF between the suggested methodology and other commonly used methods such as GA, ACA, p-q method, SRF, and other controllers mentioned in the existing literature. The data demonstrate that the suggested approach has much lower THD and higher PF in comparison to existing techniques. The PPF-EHSA optimized ANFIS enhances the system's efficiency by minimizing error and improving the adjustment capability of the UPQC. Table 3 presents the comparison of the MSE values obtained from the algorithms. The data demonstrate that the proposed approach yields

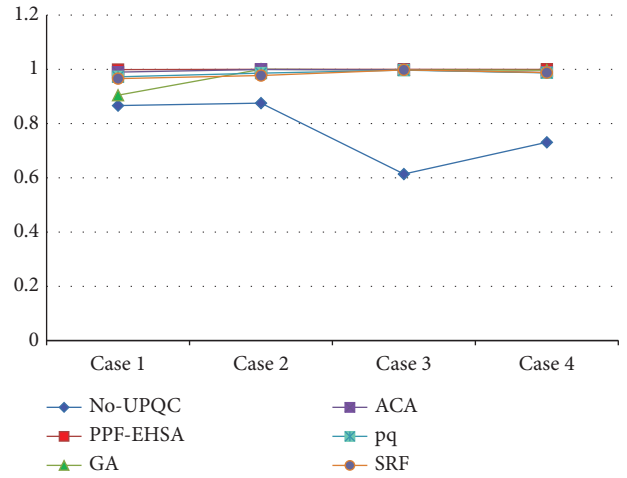

Figure 17: PF comparison for case studies.

Table 3: MSE comparison.

Case	Method	MSE
1	GA	0.02186
	ACA	0.02422
	PPF-EHSA	**0.02107**
2	GA	0.01758
	ACA	0.017214
	PPF-EHSA	**0.01274**
3	GA	0.01754
	ACA	0.01387
	PPF-EHSA	**0.01107**
4	GA	0.07214
	ACA	0.07851
	PPF-EHSA	**0.00358**

Bold values indicate and highlight the best as well as the proposed model result.

Table 4: Optimized filter parameter values of proposed PPF-EHSA.

Case	R_{se}	L_{se}	R_{sh}	L_{sh}
1	2.001	2.645	0.478	0.510
2	6.342	1.021	0.025	6.315
3	5.774	4.074	0.101	8.728
4	0.897	8.105	0.012	1.041

a lower MSE in comparison to GA and ACA techniques. In addition, the optimum values of UPQC filter parameters for the proposed system are presented in Table 4. Figure 11 demonstrates that the proposed PPF-EHSA achieves a lower MSE in a smaller number of iterations (22), indicating faster convergence compared to GA (45) and ACA (39). Figure 18 depicts the FFT analysis of the proposed system for case study 4. Furthermore, based on the findings presented in Figure 19, the implemented strategies demonstrate their ability to rapidly stabilize the DCLV in a brief duration (almost less than 0.1 seconds) amidst changes in both load and irradiation. This is significantly lower compared to the effectiveness of alternative methods.

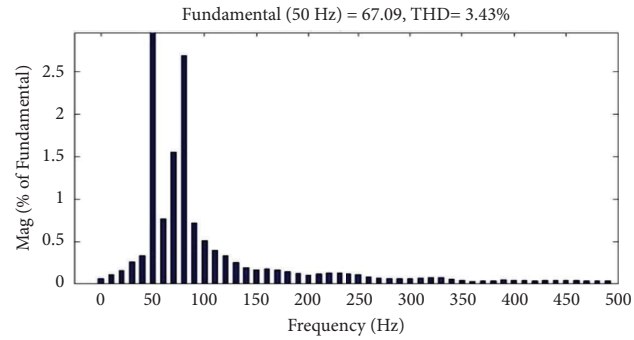

Figure 18: THD spectrum for case 4.

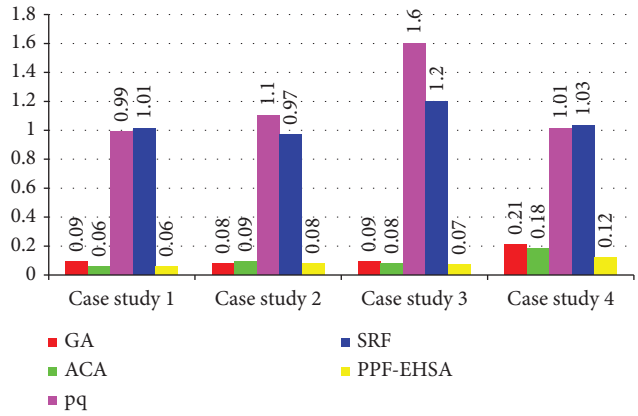

Figure 19: Time in sec taken for DLCV to reach stable.

5. Conclusion

This study presents an innovative LMBP-trained ANNC method for producing the reference signals for SBES and battery-associated UPQC to avoid the complex abc to dq0 conversions. Additionally, the PPF-EHSA algorithm is used to design the optimal MSF of ANFIS and filter parameters, with the multiobjective of decreasing both the MSE and THD. Besides, the suggested UPVBSS ensures a consistent DLCV under various conditions such as loads, sun irradiation, and temperature fluctuations. It also effectively reduces current harmonics, enhances the current waveform, hence improving the PF, and eliminates voltage fluctuations. In the future, the approach can be extended to incorporate advanced metaheuristic algorithms for the implementation of multilevel UPQC.

Appendix

Test System Specifications

The system values are PCC line voltage: 415 V, 50 Hz; DC-bus voltage: 700 V; DC-bus capacitor: 2200 μF. PV panel type: SPR-305E-WHT-D; no. of parallel strings/series module per string: 66/5; no of cells considered per each module: 96; max power obtained as output: 305.226 W;

current at output: 5.58 A; open circuit voltage: 64.2 V; short circuit current: 5.96 A.

Battery: nickel metal hydrate; nominal voltage: 500; SOC: 60%; full charge voltage: 588.983; rated capacity: 100 Ah; cut-off voltage: 37 V

Data Availability

No data were used to support the findings of this study.

Conflicts of Interest

The authors declare that they have no conflicts of interest.

References

[1] D. Yang, Z. Ma, X. Gao, Z. Ma, and E. Cui, "Control strategy of intergrated photovoltaic-UPQC system for DC-bus voltage stability and voltage sags compensation," *Energies*, vol. 12, no. 20, p. 4009, 2019.

[2] F. Nkado, F. Nkado, I. Oladeji, and R. Zamora, "Optimal design and performance analysis of solar PV integrated UPQC for distribution network," *European Journal of Electrical Engineering and Computer Science*, vol. 5, no. 5, pp. 39–46, 2021.

[3] S. Vinnakoti and V. R. Kota, "ANN based control scheme for a three-level converter based unified power quality conditioner," *Journal of electrical systems and information technology*, vol. 5, no. 3, pp. 526–541, 2018.

[4] H. Mahar, H. M. Munir, J. B. Soomro et al., "Implementation of ANN controller based UPQC integrated with microgrid," *Mathematics*, vol. 10, no. 12, p. 1989, 2022.

[5] V. V. Nagireddy, V. R. Kota, and D. V. Ashok Kumar, "Hybrid fuzzy back-propagation control scheme for multilevel unified power quality conditioner," *Ain Shams Engineering Journal*, vol. 9, no. 4, pp. 2709–2724, 2018.

[6] Y. Hoon, M. Mohd Radzi, M. Hassan, and N. Mailah, "Control algorithms of shunt active power filter for harmonics mitigation: a review," *Energies*, vol. 10, no. 12, p. 2038, 2017.

[7] P. Cholamuthu, B. Irusappan, S. Kumar Ramu et al., "A grid-connected solar PV/wind turbine based hybrid energy system using ANFIS controller for hybrid series active power filter to improve the power quality," *International Transactions on Electrical Energy Systems*, vol. 2022, p. 14.

[8] T. Lei, N.Z. SaleemRiaz, F.P. MuniraBatool, and S. Zhang, "Performance analysis of grid-connected distributed generation system integrating a hybrid wind-PV farm using UPQC," *Complexity*, vol. 2022, Article ID 9374638, 14 pages, 2022.

[9] O. E. Okwako, Z.-H. Lin, M. Xin, K. Premkumar, and A. J. Rodgers, "Neural network controlled solar PV battery powered unified power quality conditioner for grid connected operation," *Energies*, vol. 15, no. 18, p. 6825, 2022.

[10] A. K. Mishra, S. R. Das, P. K. Ray, R. K. Mallick, A. Mohanty, and D. K. Mishra, "PSO-GWO optimized fractional order PID based hybrid shunt active power filter for power quality improvements," *IEEE Access*, vol. 8, pp. 74497–74512, 2020.

[11] K. Chandrasekaran, J. Selvaraj, C. R. Amaladoss, and L. Veerapan, "Hybrid renewable energy based smart grid system for reactive power management and voltage profile enhancement using artificial neural network," *Energy Sources, Part A: Recovery, Utilization, and Environmental Effects*, vol. 43, no. 19, pp. 2419–2442, 2021.

[12] K. Srilakshmi, K. Krishna Jyothi, G. Kalyani, and Y. Sai Prakash Goud, "Design of UPQC with solar PV and battery storage systems for power quality improvement," *Cybernetics and Systems*, pp. 1–30, 2023.

[13] K. Sarker, D. Chatterjee, and S. K. Goswami, "A modified PV-wind-PEMFCS-based hybrid UPQC system with combined DVR/STATCOM operation by harmonic compensation," *International Journal of Modelling and Simulation*, vol. 41, no. 4, pp. 243–255, 2020.

[14] Y. Hoon, M. A. Mohd Radzi, M. A. A. Mohd Zainuri, and M. A. M. Zawawi, "Shunt active power filter: a review on phase synchronization control techniques," *Electronics*, vol. 8, no. 7, p. 791, 2019.

[15] M. Nicola, C. I. Nicola, D. Sacerdoțianu, and A. Vintilă, "Comparative performance of UPQC control system based on PI-gwo, fractional order controllers, and reinforcement learning agent," *Electronics*, vol. 12, no. 3, p. 494, 2023.

[16] S. J. Alam, S. R. Arya, and R. K. Jana, "Biogeography based optimization strategy for UPQC PI tuning on full order adaptive observer based control," *IET Generation, Transmission and Distribution*, vol. 15, no. 2, pp. 279–293, 2021.

[17] U. K. Renduchintala, C. Pang, K. M. Tatikonda, and L. Yang, "ANFIS-Fuzzy logic based UPQC in interconnected microgrid distribution systems: modeling, simulation and implementation," *Journal of Engineering*, vol. 2021, no. 1, pp. 6–18, 2021.

[18] P. Rajesh, F. H. Shajin, and L. Umasankar, "A novel control scheme for PV/wt/FC/battery to power quality enhancement in micro grid system: a hybrid technique," *Energy Sources, Part A: Recovery, Utilization, and Environmental Effects*, vol. 17, 2021.

[19] C. Pazhanimuthu and S. Ramesh, "Grid integration of renewable energy sources (RES) for power quality improvement using adaptive fuzzy logic controller based series hybrid active power filter (SHAPF)," *Journal of Intelligent and Fuzzy Systems*, vol. 35, no. 1, pp. 749–766, 2018.

[20] K. Srilakshmi, C. N. Sujatha, P. K. Balachandran, L. Mihet-Popa, and N. U. Kumar, "Optimal design of an artificial intelligence controller for solar-battery integrated UPQC in three phase distribution networks," *Sustainability*, vol. 14, no. 21, p. 13992, 2022.

[21] H. Kenjrawy, C. Makdisie, I. Houssamo, and N. Mohammed, "New modulation technique in smart grid interfaced multilevel UPQC-PV controlled via fuzzy logic controller," *Electronics*, vol. 11, no. 6, p. 919, 2022.

[22] K. Srilakshmi, N. Srinivas, P. K. Balachandran et al., "Design of soccer league optimization based hybrid controller for solar-battery integrated UPQC," *IEEE Access*, vol. 10, pp. 107116–107136, 2022.

[23] S. Vinnakoti and V. Reddy Kota, "Implementation of artificial neural network based controller for a five-level converter based UPQC," *Alexandria Engineering Journal*, vol. 57, pp. 1475–1488, 2017.

[24] X. Xie and Y. Sun, "A piecewise probabilistic harmonic power flow approach in unbalanced residential distribution systems," *International Journal of Electrical Power and Energy Systems*, vol. 141, 2022.

[25] C. Yang, Z. Wu, X. Li, and A. Fars, "Risk-constrained stochastic scheduling for energy hub: integrating renewables, demand response, and electric vehicles," *Energy*, vol. 288, 2024.

[26] X. Lin, Y. Liu, J. Yu, R. Yu, J. Zhang, and H. Wen, "Stability analysis of Three-phase Grid-Connected inverter under the weak grids with asymmetrical grid impedance by LTP theory

in time domain," *International Journal of Electrical Power and Energy Systems*, vol. 142, 2022.

[27] X. Zhang, Z. Wang, and Z. Lu, "Multi-objective load dispatch for microgrid with electric vehicles using modified gravitational search and particle swarm optimization algorithm," *Applied Energy*, vol. 306, 2022.

[28] Y. Duan, Y. Zhao, and J. Hu, "An initialization-free distributed algorithm for dynamic economic dispatch problems in microgrid: modeling, optimization and analysis," *Sustainable Energy, Grids and Networks*, vol. 34, 2023.

[29] M. Shirkhani, J. Tavoosi, S. Danyali et al., "A review on microgrid decentralized energy/voltage control structures and methods," *Energy Reports*, vol. 10, pp. 368–380, 2023.

[30] B. Zhu, Y. Sun, J. Zhao, J. Han, P. Zhang, and T. Fan, "A critical scenario search method for intelligent vehicle testing based on the social cognitive optimization algorithm," *IEEE Transactions on Intelligent Transportation Systems*, vol. 24, no. 8, pp. 7974–7986, 2023.

[31] Y. Wang, P. Chen, J. Yong, W. Xu, S. Xu, and K. Liu, "A comprehensive investigation on the selection of high-pass harmonic filters," *IEEE Transactions on Power Delivery*, vol. 37, no. 5, pp. 4212–4226, 2022.

[32] D. Rekioua, Z. Mokrani, K. Kakouche et al., "Optimization and intelligent power management control for an autonomous hybrid wind turbine photovoltaic diesel generator with batteries," *Scientific Reports*, vol. 13, no. 1, 2023.